Discrete modeling of concrete failure and size-effect

Madura Pathirage, Danyang Tong, Flavien Thierry, Gianluca Cusatis, David Grégoire, Gilles Pijaudier-Cabot

Discrete modeling of concrete failure and size-effect

Madura Pathirage[a,b], Danyang Tong[a], Flavien Thierry[b], Gianluca Cusatis[a], David Grégoire[b,c], Gilles Pijaudier-Cabot[b,c]

[a] *Department of Civil and Environmental Engineering, Northwestern University, Evanston, IL, USA.*
[b] *Universite de Pau et des Pays de l'Adour, E2S UPPA, CNRS, TotalEnergies, LFCR, Anglet, France.*
[c] *Institut Universitaire de France, Paris, France.*

Abstract

–

Accepted manuscript in *Theoretical and Applied Fracture Mechanics.*

DOI: 10.1016/j.tafmec.2022.103738.

The final publication is available at:

https://doi.org/10.1016/j.tafmec.2022.103738.

–

Size-effect in concrete and other quasi-brittle materials defines the relation between the nominal strength and structural size when material fractures. The main cause of size-effect is the so-called energetic size-effect which results from the release of the stored energy in the structure into the fracture front. In quasi-brittle materials and in contrast to brittle materials, the size of the fracture process zone is non-negligible compared to the structural size. As a consequence, the resulting size-effect law is non-linear and deviates from the response predicted by linear elastic fracture mechanics. In order to simulate the size-effect, one needs to rely on numerical modeling to describe the formation, development and propagation of the fracture process zone. Although a number of models have been proposed over the years, it transpires that a correct description of the fracture and size-effect which accounts for boundary effects and varying structural geometry remains challenging. In this study, the Lattice Discrete Particle Model (LDPM) is proposed to investigate the effects of structural dimension and geometry on the nominal strength and fracturing process in concrete. LDPM simulates concrete at the aggregate level and has shown superior capabilities

in simulating complex cracking mechanisms thanks to the inherent discrete nature of the model. In order to evaluate concrete size-effect and provide a solid validation of LDPM, one of the most complete experimental data set available in the literature was considered and includes three-point bending tests on notched and unnotched beams. The model parameters were first calibrated on a single size notched beam under three-point bending and on the mechanical response under unconfined compression. LDPM was then used to perform blind predictions on the load-crack mouth opening displacement curves of different beam sizes and notch lengths. Splitting test results on cylinders were also predicted. The results show a very good agreement with the experimental data. The quality of the predictions was quantitatively assessed. In addition, a discussion on the fracturing process and dissipated energy is provided. Last but not least, the Universal Size-Effect Law proposed by Bažant and coworkers was used to estimate concrete fracture parameters based on experimental and numerical data.

Keywords: Concrete failure, Size-effect, Effect of geometry, Lattice Discrete Particle Model, Numerical modeling, Energy dissipation

1. Introduction

Size-effect in quasi-brittle materials has been extensively investigated in the literature experimentally, theoretically, and numerically. In these materials, a reduction in strength is observed when the structural size increases in geometrically similar structures. This phenomenon has been confirmed for concrete (see for instance the work of Bažant and Pfeiffer (1987); Hoover et al. (2013); Grégoire et al. (2013); Çağlar and Şener (2016)) and its importance was acknowledged in the civil engineering community, as it was for the first time incorporated in the most recent ACI standard in 2019 (ACI-Committee, 2019). Two main reasons explain this size-effect (Bažant and Planas, 1997; Bažant, 2002; Bažant and Le,

*Corresponding author: Gilles Pijaudier-Cabot, Universite de Pau et des Pays de l'Adour, E2S UPPA, CNRS, TotalEnergies, LFCR. Address: Allée du parc Montaury - 64600 Anglet, France. Email: gilles.pijaudier-cabot@univ-pau.fr

2017). The first one is the redistribution of stress due to stable crack propagation and release of stored energy into the fracture front. The second reason is the spatial randomness in material properties. In this study, only size-effect due to stress redistribution is studied, i.e. the energetic size-effect which is, in passing, purely deterministic. In concrete, the size of the fracture process zone (FPZ) is non-negligible as compared to the structural size and a complete non-linear theoretical fracture mechanics framework does not exist. Simplified analytical formulations such as Bažant's size-effect law (Bažant, 2002) only provide an approximate description of concrete scaling law. In order to account for the release of the stored energy in the FPZ, and for the development and propagation of the fracture front for different specimen sizes and shapes, one must carry out accurate numerical simulations. Several types of models have been proposed over the years to describe concrete fracture and size-effect. One can mention for instance the cohesive model (Elices et al., 2002), the crack-band model (Bažant and Oh, 1983), non-local continuum damage models (Bažant and Jirásek, 2002), and discrete models (Bolander et al., 2021). In all the aforementioned formulations, two features are essential in capturing size-effect in strain softening materials such as concrete: (i) crack localization and (ii) existence of an internal characteristic length related to the size of the heterogeneity. In continuum models, these two ingredients are phenomenologically defined through constitutive laws. In this respect, random lattice or particle models such as the ones described by Cusatis et al. (2011a) or Eliáš et al. (2015) are considered superior. The actual mix design and particle size distribution can be simulated to produce a realistic heterogeneous internal structure made of interacting aggregates. In addition, the randomness in spatial distribution of particles reproduces the statistically isotropic nature of concrete and eliminates directional mesh bias during the fracturing process. Finally, a recent argument in favor of lattice particle models is their ability to capture the effect of stress parallel to cracks on the FPZ size and the induced size-effect, which was demonstrated to be significant in concrete (Nguyen et al., 2020a,b). In this study, one of such models, namely the Lattice Discrete Particle Model (LDPM) (Cusatis et al., 2011a,b) which simulates concrete at the coarse aggregate level is adopted.

In order to assess the capabilities of LDPM in simulating fracture and predicting size-

effect, a comprehensive experimental data set on concrete fracturing (Grégoire et al., 2013) was considered in this study. This data set is among one of the very few available in the literature that includes three-point bending tests on notched and unnotched beams and encompasses a large range of beam depths. It should be mentioned that this set of data was previously used in several studies involving other numerical models. More specifically, an integral-type non-local model was used but was found ineffective in capturing correct size and geometry effects (Grégoire et al., 2013). In another study, a lattice model (Grassl et al., 2012) was able to simulate the data with a good accuracy. It must however be noted that the latter model falls into the miniscale category which implies computationally prohibitive simulations for more complex geometries that require an increase in structural size or account for the third dimension in the out-of-plane direction. It should also be mentioned that the model used in that study was bidimensional and that to the authors knowledge, there has been no attempt to extend the simulations to the 3D case. More recently, a study proposed to simulate concrete fracturing using a local isotropic damage constitutive model of the Rankine type through the crack band model (Barbat et al., 2020). Although a good agreement with experimental data was found, this type of smeared crack model is limited in capturing complex cracking mechanisms and realistic crack tortuosity observed in concrete, which might have a non-negligible effect on energy dissipation during fracture. As a matter of fact, this effect is especially important in the case of unnotched beams where a large damage zone is generated before its collapse to a single propagating crack that is ultimately tortuous and not straight. Last but not least, a re-implementation of LDPM which includes stochasticity in material parameters was recently used to simulate the data used in this paper (Eliáš and Vořechovskỳ, 2020) with a very good accuracy. It should be however emphasized that the latter study did not assess the capability of the model to predict size-effect. Indeed, the study used all the load-crack mouth opening displacement (CMOD) curves for all the beam sizes and notch lengths in the calibration process, with the exception of the unnotched beams and the smallest sizes that were discarded.

In this work, the relevant LDPM parameters were calibrated on a single beam configuration, leaving the remaining fracture test results for blind predictions, including splitting

tests. In addition and in contrast with most available studies, a rigorous quantification of the prediction accuracy was performed. It is the wish of the authors that this work would, to some extent, pave the way for more detailed and quantitative analyses of goodness of fits and prediction quality in future numerical studies within the concrete community, using the same set of experimental data but possibly other data. This would ultimately allow one to compare different model capabilities, develop the most effective models and abandon the less accurate ones. The proposed approach and preliminary results were presented in a recent conference (Pathirage et al., 2022b,a; Pijaudier-Cabot et al., 2022). They are here largely extended and commented.

2. The Lattice Discrete Particle Model

In order to simulate the FPZ formation and propagation in concrete necessary to capture size-effect, the Lattice Discrete Particle Model is here adopted. This model originally proposed by Cusatis and coworkers (Cusatis et al., 2011a,b) simulates the mechanical interactions among major material heterogeneities, i.e. coarse aggregates in concrete. Over the years, this model has been used to simulate other granular quasi-brittle materials such as mortar (Pathirage et al., 2019b; Han et al., 2020), fiber reinforced concrete and engineered cementitious composites (Schauffert and Cusatis, 2011; Rezakhani et al., 2021; Feng et al., 2022), unreinforced and reinforced stone masonry (Mercuri et al., 2020; Angiolilli et al., 2020, 2021; Mercuri et al., 2022, 2021), shale (Li et al., 2017), or cycling in concrete (Zhu et al., 2022). LDPM was also coupled to multi-physics models describing cement hydration from microscale simulations, heat transfer and mositure diffusion, alkali-silica reaction, creep, aging (Alnaggar et al., 2013; Pathirage et al., 2019a; Yang et al., 2021, 2022), or more recently self-healing in concrete (Cibelli et al., 2022).

2.1. Internal geometry

In order to generate the LDPM skeleton, spherical particles are placed in a volume of material from the largest to smallest size. This placement follows a prescribed particle size distribution that is based on the actual concrete mix design with the maximum and minimum

aggregate sizes, d_a and d_0, respectively. Figure 1(a) shows an example of particle placement in a prismatic sample. In order to simulate the interaction between particles, a lattice system is generated by means of a Delaunay tetrahedralization with the centers of particles. A dual tessallation is then performed which finally produces a system of polyhedral cells enclosing the spherical particles. Figure 1(b) shows an example of two adjacent polyhedral cells enclosing the spherical particles. One can also refer to Figures 22(b)-(d) where cells at the surface of prismatic samples are depicted. The surface of each polyhedral cell is composed of triangular facets where failure can potentially occur. On each facet, stresses and strains are formulated in a vectorial form through constitutive equations. Figure 1(c) shows the three unit vectors defined at a generic facet colored in red, in the normal direction and in the two tangential directions. LDPM incorporates specific constitutive equations to describe tensile fracturing with strain softening, cohesive and frictional shearing, and compressive response with strain-hardening. Since this study focuses on concrete fracturing, the corresponding constitutive laws are detailed in the following. The reader is referred to the Appendix for the complete set of constitutive equations.

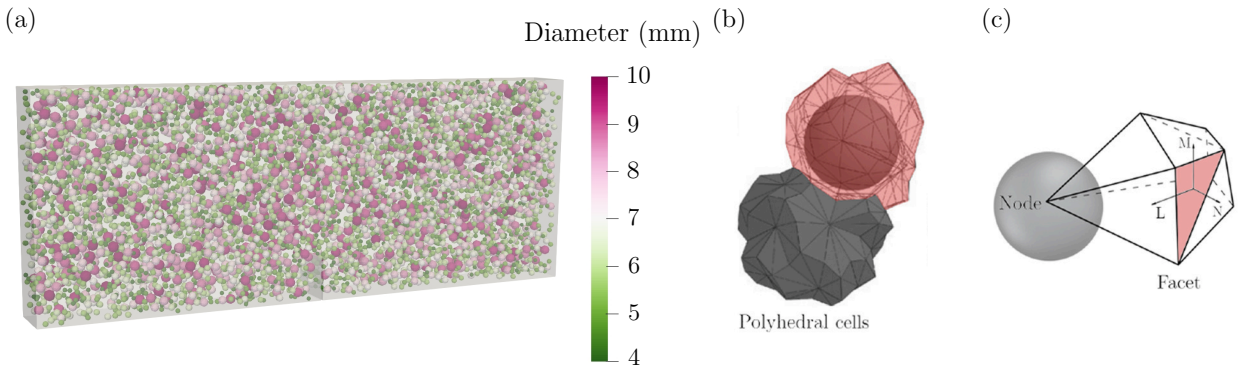

Figure 1: LDPM internal geometry: (a) particle placement in a prismatic volume, (b) two adjacent LDPM cells, and (c) triangular facet and vector orientations.

2.2. Elastic, tension, and tension-shear constitutive behaviors

If $\mathbf{x}_i$ and $\mathbf{x}_j$ denote the positions of nodes i and j, adjacent to the facet k, the facet strains are defined as:

$$\mathbf{e}_k = [e_{N_k}\ e_{M_k}\ e_{L_k}]^t = \left[\frac{\mathbf{n}_k^t[\![\mathbf{u}_k]\!]}{l_k}\ \frac{\mathbf{m}_k^t[\![\mathbf{u}_k]\!]}{l_k}\ \frac{\mathbf{l}_k^t[\![\mathbf{u}_k]\!]}{l_k}\right]^t \tag{1}$$

where e_{N_k} is the normal strain component, and e_{M_k} and e_{L_k} are the tangential strain components, $[\![\mathbf{u}_k]\!] = \mathbf{u}_j - \mathbf{u}_i$ is the displacement jump corresponding to facet k, $l_k = \|\mathbf{x}_j - \mathbf{x}_i\|$ is the distance between the two nodes, $\mathbf{n}_k = (\mathbf{x}_j - \mathbf{x}_i)/l_k$ and $\mathbf{m}_k$ and $\mathbf{l}_k$ are two unit vectors mutually orthogonal in the facet plane projected orthogonally to the line connecting the adjacent nodes. The traction vector is defined as $\mathbf{t}_k = [t_{N_k}\ t_{M_k}\ t_{L_k}]^t$, where t_{N_k} is the normal component, and t_{M_k} and t_{L_k} are the shear components. For the sake of readability, the subscript k that designates the facet is dropped. The elastic behavior is formulated through linear relations between the normal and shear stresses, and the corresponding strains as follows:

$$t_N = E_N e_N\ ,\ t_M = E_T e_M\ ,\ t_L = E_T e_L \tag{2}$$

where $E_N = E_0$ and $E_T = \alpha_0 E_0$. $E_0 \approx E/(1-2\nu)$ and $\alpha_0 \approx (1-4\nu)/(1+\nu)$ are the effective normal modulus and the shear-normal coupling parameter, respectively, and E is the macroscopic Young's modulus and ν is the macroscopic Poisson's ratio.

Because of the mesoscale nature of the model, concrete fracturing in mode I opening is always accompanied by shear at facets. This is a realistic feature since it is experimentally observed that most fracture paths are located at the interface between aggregates and cement paste. Therefore, the cohesive fracture behaviors in tension but also in tension-shear are important. This cohesive fracture occurs for $e_N > 0$. One can define an effective strain as $e = (e_N^2 + \alpha_0(e_M^2 + e_L^2))^{\frac{1}{2}}$, and an effective stress as $t = (t_N^2 + (t_M^2 + t_L^2)/\alpha_0)^{\frac{1}{2}}$ and write the relationship between stresses and strains through $t_N = te_N/e$, $t_M = \alpha_0 te_M/e$ and $t_L = \alpha_0 te_L/e$. The effective stress t is defined incrementally as $\dot{t} = E_N\dot{e}$ and its magnitude is limited by a strain-dependent boundary which is written as $0 \leqslant t \leqslant \sigma_{bt}(e, \omega_{sn})$ where

$$\sigma_{bt}(e, \omega_{sn}) = \sigma_0(\omega_{sn}) \exp\left[-H_0(\omega_{sn})\frac{\langle e_{\max} - e_0(\omega_{sn})\rangle}{\sigma_0(\omega_{sn})}\right] \tag{3}$$

$\langle x \rangle = \max(x, 0)$, ω_{sn} is a variable defining the level of interaction between shear and normal loadings. It is defined as $\tan(\omega_{sn}) = (e_N)/(\sqrt{\alpha_0} e_T) = (t_N \sqrt{\alpha_0})/(t_T)$ where e_T is the total shear strain $e_T = (e_M^2 + e_L^2)^{\frac{1}{2}}$, and t_T is the total shear stress $t_T = (t_M^2 + t_L^2)^{\frac{1}{2}}$. The maximum effective strain is time dependent and is defined as $e_{\max}(\tau) = (e_{N,\max}^2(\tau) + \alpha_0 e_{T,\max}^2(\tau))^{\frac{1}{2}}$ where $e_{N,\max}(\tau) = \max_{\tau' < \tau}[e_N(\tau')]$ and $e_{T,\max}(\tau) = \max_{\tau' < \tau}[e_T(\tau')]$. The strength limit of the effective stress that defines the transition between pure tension and pure shear is written as

$$\sigma_0(\omega_{sn}) = \sigma_t \frac{-\sin(\omega_{sn}) + (\sin^2(\omega_{sn}) + 4\alpha_0 \cos^2(\omega_{sn})/r_{st}^2)^{\frac{1}{2}}}{2\alpha_0 \cos^2(\omega_{sn})/r_{st}^2} \tag{4}$$

where $r_{st} = \sigma_s/\sigma_t$ is the ratio of the shear strength to the tensile strength, σ_s is the shear strength and σ_t is the tensile strength. The post-peak softening modulus is controlled by the effective softening modulus $H_0(\omega_{sn}) = H_s/\alpha_0 + (H_t - H_s/\alpha_0)\,(2\omega_{sn}/\pi)^{n_t}$, in which $H_t = 2E_0/(l_t/l - 1)$, $H_s = r_s E_0$ and n_t is the softening exponent. Typically, the values of $n_t = 0.2$ and $r_s = 0$ are assumed and are fixed. l_t is the tensile characteristic length defined as $l_t = 2E_0 G_t/\sigma_t^2$ and G_t is the mesoscale fracture energy.

2.3. Static equilibrium equations and numerical implementation

Finally, one can write the static linear and angular momentum equilibrium equations of each LDPM cell as follows:

$$\sum_{k \in \mathcal{F}_I} A_k^p \mathbf{t}_k = \mathbf{0} \ , \ \sum_{k \in \mathcal{F}_I} A_k^p \mathbf{c}_k \times \mathbf{t}_k = \mathbf{0} \tag{5}$$

where $\mathcal{F}_I$ is the set containing all the facets of a generic polyhedral cell I, $A_k^p = A_k \mathbf{n}^t \mathbf{n}_k$ is the area of the projected facet k, $\mathbf{n}$ is the orientation of the tetrahedron edge associated to facet k and $\mathbf{n}_k$ is the unit vector orthogonal to facet k of area A_k (Cusatis et al., 2011a). $\mathbf{c}_k$ is the vector that represents the distance between the center of facet k and the center of the cell. The model was implemented within a dynamic explicit scheme, with a central difference algorithm for time integration. Although the actual equations that are solved numerically are dynamic (see Cusatis et al. (2011a) for more details), the inertia terms are absent in the two expressions in Equation 5 because all the simulations presented next were performed under quasi-static conditions. In other words, loading rates were small enough to ensure

the kinetic energy in the system would not exceed 5% of the internal energy throughout the analysis.

3. Regression statistics

Before describing the modeling and calibration process, it is important to introduce the regression statistics used in this work to perform the model parameter identification and list the different statistical indicators used to assess the quality of fit and the quality of predictions. In this study, a frequentist approach is proposed.

3.1. Experimental data and model response

Let $\mathbf{y}_k^j$ be the experimental results for replicate k for a given test j. For instance, $\mathbf{y}_1^j$, $\mathbf{y}_2^j$, and $\mathbf{y}_3^j$ can be the measured forces for three replicates of a three-point bending test denoted j. In order to compare the experimental data, one needs at some point to compute the arithmetic difference between experimental data and model response $\mathbf{Y}_k^j$ as $\boldsymbol{\varepsilon}_k^j = \mathbf{y}_k^j - \mathbf{Y}_k^j$. This expression implies that a model response, which depends on the given spatial distribution of particles, corresponds to a specific replicate of the experimental test. This is not entirely correct since the internal structure of the experimentally tested material is only statistically replicated by the model.

To overcome this problem, a solution consists in: (i) averaging the experimental results of all replicates to obtain the mean data $\mathbf{y}^j$, (ii) running multiple simulations with different spatial distributions of particles and averaging the model responses to get $\mathbf{Y}^j$, and (iii) comparing the experimental and numerical results in terms of mean responses. In this process, there is a loss of information since the variance of the data is not known. Such a task would require the use a true stochastic model which appears unnecessary with respect to the very good results presented in Section 5. In addition, this loss remains minimal as the interest in this work is on central range statistics, viz. mean values for normally distributed regression errors, and is reduced as the number of replicates increases.

3.2. Parameter estimation

Let $\mathbf{x}^j$ be the predictor variable, for instance the displacements corresponding to the forces $\mathbf{y}^j$ or $\mathbf{Y}^j$. One can first discretize in equally spaced intervals the predictor variable over its range of values and define x_i^j, y_i^j, and Y_i^j at index $i = 1, ..., n^j$ where n^j is the number of discretized points. Next, if one denotes f^j the model response corresponding to the simulation of test j and $\boldsymbol{\theta} = [\theta_1 \ ... \ \theta_p]^t$ the parameter vector containing the p unknown model parameters to be estimated, then, $Y_i^j = f^j(x_i^j, \boldsymbol{\theta})$. Next, one can formulate the general minimization problem as follows:

$$\text{Find the least square estimate } \hat{\boldsymbol{\theta}} \text{ which minimizes } S^j = \sum_{i=1}^{n^j} \left(y_i^j - f^j(x_i^j, \boldsymbol{\theta})\right)^2 \tag{6}$$

where S^j is the residual sum of squares for curve j. Using the least-square method is here well justified as the conditional variance of the data used later on can be considered uniform and because the residuals of the regression $\varepsilon_i^j = y_i^j - f^j(x_i^j, \boldsymbol{\theta})$ can be generally assumed independent or non-correlated.

In the case of a single test, i.e. $j = 1$, the formulas stated earlier can be directly applied and S^1 can be minimized to obtain $\hat{\boldsymbol{\theta}}$. When multiple tests are considered simultaneously in the parameter identification process, one needs to normalize the residual sum of squares for each test and generate a global objective function to be minimized. This can be done by defining a new residual ϕ^j for each test j as follows:

$$\phi^j = \frac{S^j}{\sum_{i=1}^{n^j} \left(y_i^j\right)^2} \tag{7}$$

It is interesting to note that the normalization in Equation 7 becomes the Mean Absolute Percentage Error (MAPE) in the case of a single point estimate ($i = n^j = 1$).

The global residual is defined as a linear combination of ϕ^j for different tests j, which is consistent with the additive property of the square of the coefficient of variation of errors defined in Section 3.3. The general minimization problem is written as follows:

$$\text{Find the least square estimate } \hat{\boldsymbol{\theta}} \text{ which minimizes } \psi = \sum_{j=1}^{N} w^j \phi^j \tag{8}$$

where w^j can be seen as the weights for each test j and take the values between 0 and 1 such that $\sum_{j=1}^{N} w^j = 1$. N is the total number of tests considered. In absence of specific information about the tests, one can assume equal weights, i.e. $\forall j, w^j = 1/N$.

3.3. Fit and prediction quality

Once the estimate $\hat{\boldsymbol{\theta}}$ is obtained, one can appreciate the fit and prediction quality for each individual test. For this purpose, two statistical indicators are introduced and will be used throughout the paper.

The first indicator is the coefficient of variation of the regression errors ω^j which characterizes the ratio of the scatter band width to the data mean

$$\omega^j = \frac{s^j}{\bar{y}^j} \text{ where } s^j = \sqrt{\frac{S^j}{n^j - p}} \tag{9}$$

s^j is the standard error of the regression, $n^j - p$ is called degrees of freedom, and $\bar{y}^j = \left(\sum_{i=1}^{n^j} y_i^j\right)/n^j$ is the data mean.

The second one is the adjusted $(r^2)^j$, also called the coefficient of determination which characterizes the ratio of the scatter band width to the overall spread of data and indicates what percentage of data variation is accounted for by the model response. By defining the corrected total sum of squares $S_c^j = \sum_{i=1}^{n^j} \left(y_i^j - \bar{y}^j\right)^2$ and the standard deviation of all data $\bar{s}^j = \sqrt{S_c^j/(n^j - 1)}$, this indicator is written as:

$$\left(r^2\right)^j = 1 - \frac{\left(s^j\right)^2}{\left(\bar{s}^j\right)^2} \tag{10}$$

In the case of a single point estimate, i.e. $i = n^j = 1$, the aforementioned indicators are not valid. One can instead use the mean absolute percentage error which is written as $\text{MAPE}^j = 100|\varepsilon^j/y^j|$ where $\varepsilon^j = y^j - f^j(x^j, \hat{\boldsymbol{\theta}})$, $y^j = y_1^j$ and $x^j = x_1^j$.

In order to evaluate and quantify an overall quality of fit and predictions, one simply needs to regroup all data points for each test with their corresponding model responses into one global set and compute the overall coefficient of variation of errors, ω, and the overall coefficient of determination, r^2.

Let us underline that the coefficient of variation and the coefficient of determination are mathematically derived for linear model regression only and are, in theory, not valid when one performs regression or assesses quality of fit for non-linear (parameter-wise) models. Nevertheless, they are often used in practice because of the absence of clear indicator for quality of fit, aside from the standard error of regression which however is unit-dependent, is not expressed in percentage, and is not bounded. In addition, one might argue that when the model is already fitted and the problem is well-conditioned, the residual sum of squares which is originally non-linear can be linearized around the least square estimate. Therefore, close enough to the estimate and when the original and linearized residual sums of squares are close enough, the use of these statistical indicators can be justified.

4. Modeling and calibration process

4.1. Summary of experimental campaign

In the experimental work by Grégoire et al. (2013), four sizes of geometrically similar prismatic specimens with four depths $D = 50$ mm, 100 mm, 200 mm, and 400 mm, the span-to-depth ratio S/D of 2.5, and the out-of-plane thickness of 50 mm were tested in three-point bending. Unnotched and notched samples with a notch length a and the notch-to-depth ratios $\alpha = a/D = 0.5, 0.2, 0$ were tested under CMOD control to obtain a stable post-peak response. In the case of unnotched beams, the legs of the extensometer were attached to the bottom surface of the beams at a distance from mid-span of half the beam depth to ensure crack initiation between the legs. Splitting tests on cylinders were also conducted to estimate tensile strength. In complement to fracture tests, cylindrical samples were tested under unconfined compression and measurements of elastic parameters and compressive strength were obtained. More details on the experimental program are given by Grégoire et al. (2013).

4.2. LDPM internal geometry

The parameters required to construct the LDPM geometry were first identified based on the actual mix design used in the experiments. The particle size distribution was numerically

reproduced following the procedure described in Yang et al. (2022) with a cut-off size $d_0 = 4$ mm and a maximum size $d_a = 10$ mm. Figure 2(a) shows the experimental and numerical

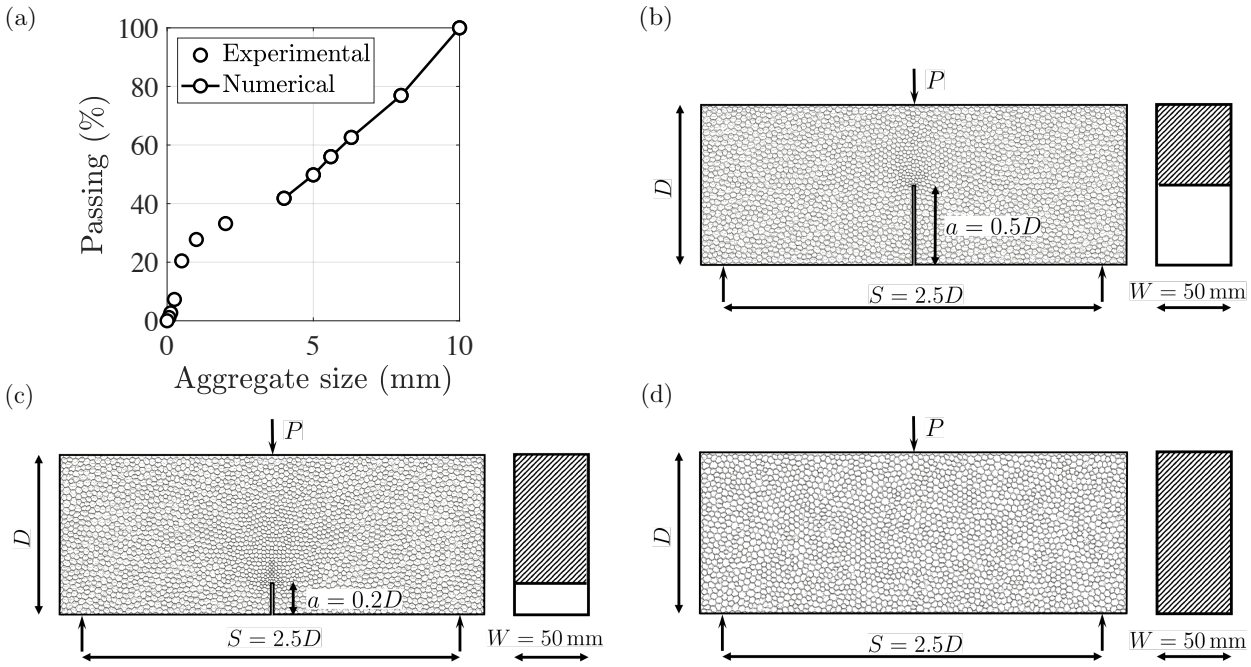

Figure 2: (a) Simulated particle size distribution, LDPM cells, geometries, and dimensions of the simulated beams with the notch-to-depth ratios of (b) 0.5, (c) 0.2, and (d) 0 viz. unotched beam, for $D = 50$ mm, 100 mm, 200 mm, and 400 mm.

sieve curves. The remaining parameters were also chosen based on the mix design: cement content $c = 286$ kg m^{-3}, water-to-cement ratio $w/c = 0.626$, and density $\rho = 2121$ kg m^{-3}. Figure 2(b)-(d) show the simulated geometries and the resulting LDPM cells at the surface of the samples.

4.3. Modeling and calibration process

The identification of the parameters in the constitutive laws describing elastic, tension, and tension-shear behaviors followed a two-step procedure. First, the normal modulus E_0 and α_0 related to the elastic behavior were calculated using the approximated formulas listed in Section 2.2, based on the mean values of the macroscopic elastic modulus and Poisson's ratio reported by Grégoire et al. (2013). The values of $E_0 = 57180$ MPa and $\alpha_0 = 0.25$ were obtained.

Next, the three parameters related to fracture and shear, i.e. the mesoscale tensile strength σ_t, the mesoscale fracture energy G_t, and the shear-to-tensile strength ratio r_{st} were identified simultaneously based on: (i) the compressive strength obtained from cylinders with the diameter $D_c = 74$ mm and the height $H_c = 142$ mm, and (ii) the entire load-CMOD curve corresponding to the medium size beam with the depth $D = 200$ mm and $\alpha = 0.2$. For the compression test, rigid plates were used on the top and bottom of the specimens. Friction between the plates and the sample was simulated through a simple Coulomb friction law with a friction coefficient $\mu = 0.13$. Concerning the bending test, the loads were applied directly on the surface nodes. Both compression and fracture tests were simulated under displacement control with a constant velocity of 1 mm s^{-1} to ensure quasi-static conditions. For each test, three simulations were performed with different spatial distributions of particles. The least square estimate of the parameter vector $\boldsymbol{\theta} = [\sigma_t \; G_t \; r_{st}]^t$ was obtained by minimizing the overall residual $\psi = \phi^{\mathrm{C}} + \phi^{\mathrm{3PBT}}$ where ϕ^{C} and ϕ^{3PBT} are the residuals computed through Equation 7 for the compression and three-point bending tests, respectively. The values of $\sigma_t = 2.9$ MPa, $G_t = 45.5$ N m^{-1}, and $r_{st} = 3.276$ were obtained.

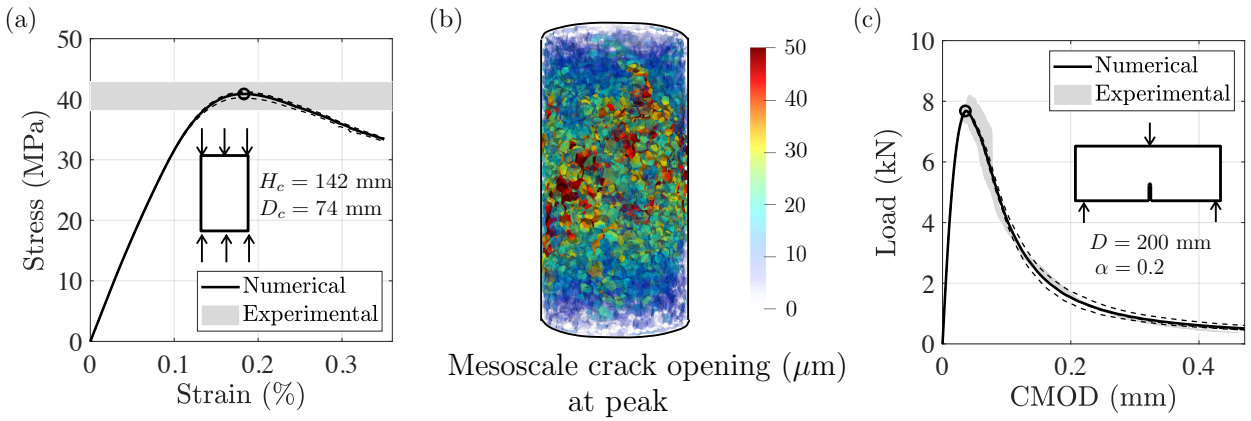

Figure 3: Calibration results: (a) stress-strain curve of the unconfined compression test on the cylinder with the diameter $D_c = 74$ mm and height $H_c = 142$ mm; the empty circle designates the mean peak value, (b) failure mode at the peak load (c) load-CMOD curve of the three-point bending test on the notched beam with $D = 200$ mm and $\alpha = 0.2$.

Figure 3(a) shows the simulated stress-strain curve of the compression test together with the compressive strength obtained experimentally. The solid line is the mean curve of

the three individual simulations represented by dashed lines. The gray area represents the experimental scatter where the upper and lower bounds of the envelope corresponds to the maximum and minimum values of loads, respectively. The mode of failure at peak is shown in Figure 3(b), characterized by a shear band. The LDPM facets are colored according to the value of the mesoscale crack opening defined as $w = (w_N^2 + w_M^2 + w_L^2)^{\frac{1}{2}}$ for $e_N > 0$ and $w = 0$ for $e_N < 0$, $w_i = l e_i^{ine}$ where $e_i^{ine} = e_i - t_i/E_i$ is the inelastic strain for $i = N, M, L$, and l is the edge length defined in Section 2.2. Figure 3(c) shows the experimental and numerical load-CMOD curves for the bending test. Typical failure modes are depicted in Figures 5(d), (e), (g) and (h). One can observe that the numerical results fit well the experimental data. In terms of quality of fit, a MAPE of 3.4% was reached for the compression test, whereas the three-point bending test fit was characterized by a coefficient of variation $\omega = 6.8\%$ and a coefficient of determination $r^2 = 0.995$. It is interesting to note that the ratio between the macroscopic splitting tensile strength f_{st} reported in Section 5.1 and the compressive strength f_c' shown in Figure 3(a) is approximately 9%, which is consistent with the range of values reported in the literature. Note also that the mesoscale tensile strength σ_t and the compressive yielding strength σ_{c0} are not macroscopic properties but only model parameters.

As explained in Section 2, concrete failure is characterized by multiple mechanisms that are different and LDPM is able to simulate all these mechanisms. For each mechanism, there is a set of relevant model parameters (less than 4) which makes the total number of parameters to be 16. The elastic behavior modeled by two parameters (E_0, α_0) and the mesoscale mixed mode fracture governed by three parameters (σ_t, G_t, r_{st}) have been identified. The remaining parameters were assumed based on the actual mix design and Section 5.3 by Cusatis et al. (2011b), namely the softening exponent n_t governing the interaction between shear and tensile behavior during softening, (σ_{c0}, H_{c0}, κ_{c0}, E_d) defining the behavior of the facet normal component under compression and affecting the macroscopic behavior in compression, (μ_0, μ_∞, σ_{N0}) contributing to the LDPM response in compression, mainly the triaxial compressive behavior at high-confinement, (κ_{c1}, κ_{c2}) governing the nonlinear evolution of the normal facet stress in compression, and finally β controlling the coupling between the mesoscale compressive behavior and the macroscopic triaxial compressive behavior. All

parameters are listed in Table 1 for the sake of clarity.

Table 1: Values of the material model parameters used in the numerical simulations

Designation	Symbol	Units	Value	Source
Density	ρ	kg m^{-3}	2338	Grégoire et al. (2013)
Water-to-cement ratio	w/c	-	0.626	Grégoire et al. (2013)
Maximum aggregate size	d_a	mm	10	Grégoire et al. (2013)
Minimum aggregate size	d_0	mm	4	Fixed
Effective normal modulus	E_0	MPa	57,180	Identified
Shear-normal coupling parameter	α_0	-	0.25	Identified
Tensile strength	σ_t	MPa	2.9	Identified
Fracture energy	G_t	N mm^{-1}	45.5	Identified
Shear strength ratio	r_{st}	-	3.276	Identified
Softening exponent	n_t	-	0.2	Cusatis et al. (2011b)
Compressive yielding strength	σ_{c0}	MPa	120	Cusatis et al. (2011b)
Initial hardening modulus ratio	H_{c0}/E_0	-	0.4	Cusatis et al. (2011b)
Transitional strain ratio	κ_{c0}	-	2	Cusatis et al. (2011b)
Deviatoric strain threshold ratio	κ_{c1}	-	1	Cusatis et al. (2011b)
Deviatoric damage parameter	κ_{c2}	-	5	Cusatis et al. (2011b)
Initial friction	μ_0	-	0.2	Cusatis et al. (2011b)
Asymtotic friction	μ_∞	-	0.0	Cusatis et al. (2011b)
Transitional stress	σ_{N0}	MPa	600	Cusatis et al. (2011b)
Densification ratio	E_d/E_0	-	1.0	Cusatis et al. (2011b)
Volumetric deviatoric coupling	β	-	0.0	Cusatis et al. (2011b)

5. Prediction results and discussion

The capability of the model to simulate fracture and predict size-effect was assessed by carrying out blind simulations, i.e. without adjusting model parameters, on splitting and size-effect tests for different beam sizes and notch lengths.

5.1. Splitting test

LDPM was first validated on splitting tests for which peak loads for nine replicates are reported by Grégoire et al. (2013). For this purpose, three cylinders with the height $L_s = 215$ mm and the diameter $D_s = 113$ mm with different spatial distributions of particles were simulated. The load was applied directly on particles at the surface of the cylinder. In addition, the simulations were performed under displacement control with a constant loading rate of 1 mm s^{-1} to ensure quasi-static conditions.

Figure 4(a) shows the mean predicted nominal stress versus displacement curve represented by a solid line and the three individual simulations in dashed lines, along with the experimental scatter represented with a gray area. The nominal strength was computed

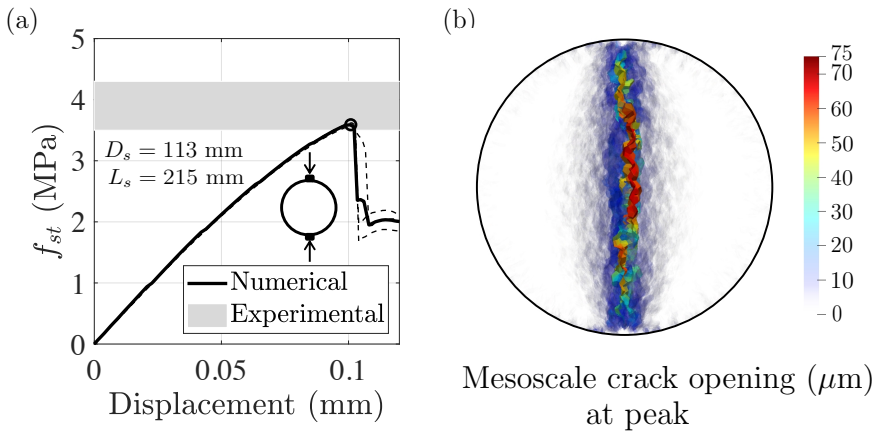

Figure 4: Prediction results: (a) nominal stress-displacement curve of the splitting test; the empty circle designates the mean peak value, and (b) failure mode at the peak load.

using the formula $f_{st} = (2P_{st,u})/(\pi D_s L_s)$ where $P_{st,u}$ is the splitting peak force. One can observe that the numerical mean splitting tensile strength is within the scatter of the experiments. A MAPE of 7.5% was found when comparing the experimental and simulation peak values, which indicates a good accuracy in the prediction with respect to the scatter observed in experiments. Figure 4(b) shows the mode of failure at the peak load. As expected and in accordance with experimental observation, fracture initiates at the center where tensile stresses are the highest. The main crack is tortuous and has a slight eccentricity with respect to the vertical line passing through the center. This is due to the inherent ability of the

mesoscale model to reproduce heterogeneity in the material, and is by the way routinely observed in experiments (Rocco, 1996; Bažant and Planas, 1997).

5.2. Size-effect tests

5.2.1. Load-CMOD curves

The model was next used to predict the load-CMOD curves for all sizes and notch lengths. The simulations were performed under displacement control and quasi-staticity was ensured by applying loads at a constant loading rate of 1 mm s^{-1}. Figures 5(a)-(c) show the predicted curves for the notch-to-depth ratios of 0.5, 0.2, and 0, respectively. The solid line is the mean response of the three individual simulations in dashed lines. The experimental scatter is represented with a gray area. One can observe that the numerical simulations predict well the mechanical behavior in the elastic, near-peak and post-peak regimes for the different geometries and sizes. The prediction in the post-peak of the smallest size beam with a notch-to-depth ratio of 0.5 deviates from the experimental results. The reason might be that the number of aggregates in the ligament is not enough and makes the model too coarse. In addition, boundary effects play a significant role for such small specimens. In the case of the two unnotched beams with largest sizes, the response stops at the peak due to snapback, similarly to what was observed in the experiments.

5.2.2. Fracture process zone and dissipated energy

Figures 5(d)-(i) show the typical failure modes for the beams with the size $D = 100$ mm for two different displacement values. Two types of failure can be distinguished. (i) For the notched specimens, the FPZ is localized and emanates at the crack tip. It develops for the increasing load and finally reaches an ultimate size at the peak load (Figures 5(d) and (e)). The FPZ of the constant size then propagates through the ligament (Figures 5(g) and (h)), which explains the strain softening behavior observed at the macroscale. (ii) For the unnotched specimens, the FPZ initiates at the bottom surface of the sample, where the stresses approach the material tensile strength, and is diffused on a zone much larger in size as compared to the notched-beam case. As the load increases up to the peak, the damaged zone

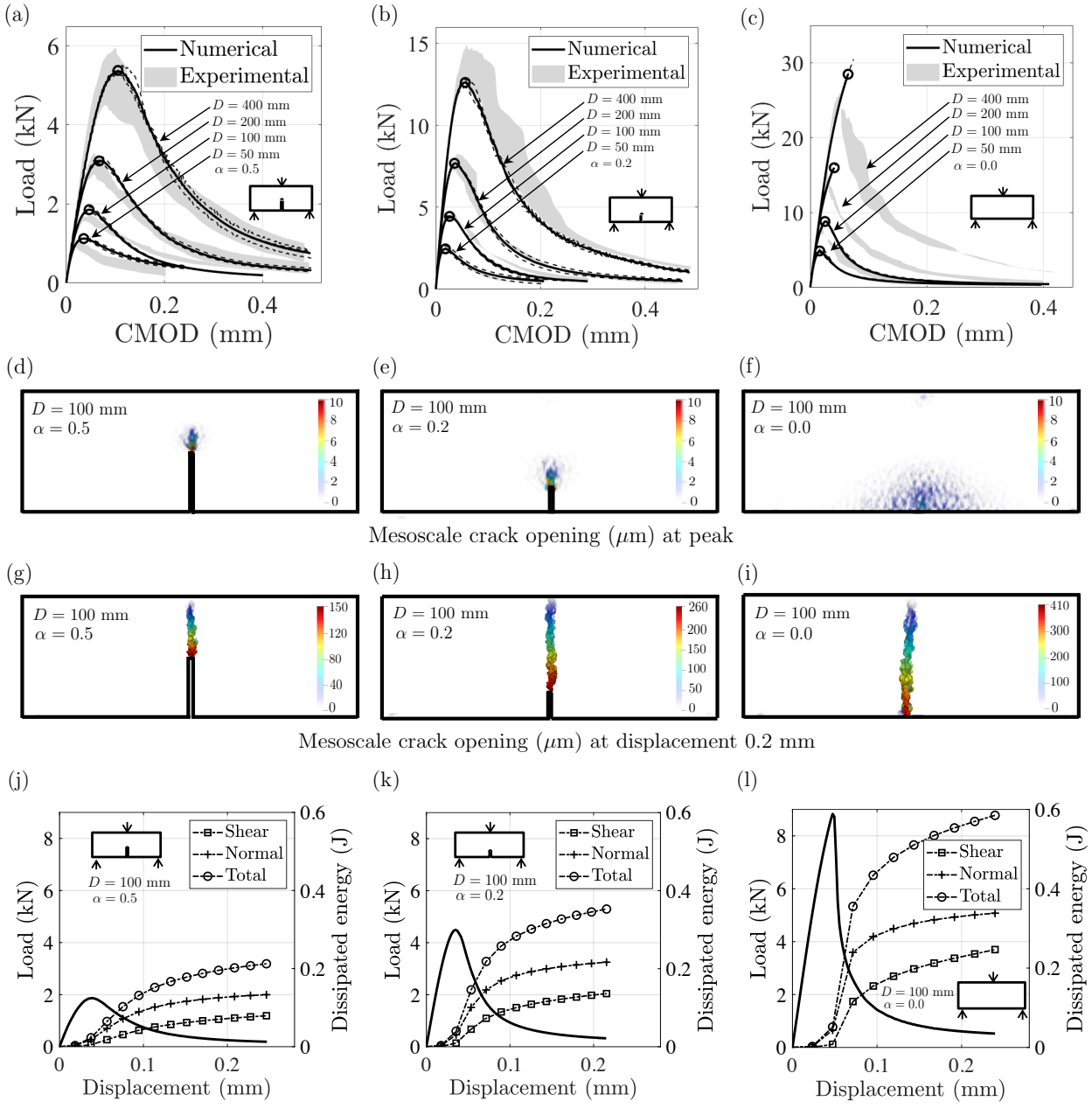

Figure 5: Prediction results: load-CMOD curves for (a) $\alpha = 0.5$, (b) $\alpha = 0.2$, (c) $\alpha = 0$, the empty circles designate mean peak values; failure modes at the peak load for the samples with the depth $D = 100$ mm for (d) $\alpha = 0.5$, (e) $\alpha = 0.2$, (f) $\alpha = 0$; failure modes at a displacement of 0.2 mm for the samples with the depth $D = 100$ mm for (g) $\alpha = 0.5$, (h) $\alpha = 0.2$, (i) $\alpha = 0$; dissipated energies for (j) $\alpha = 0.5$, (k) $\alpha = 0.2$, (l) $\alpha = 0$.

becomes larger (Figure 5(f)). At the peak load, the FPZ eventually collapses to a single crack that propagates, whereas the surrounding strained material unloads. One can also observe that the final crack does not necessarily originate at mid-span. This phenomena shows the direct effect of material heterogeneity, realistically captured by the mesoscale model. Although not quantified here, the evolution of the FPZ is consistent with the one described in Lefort et al. (2015) based on Ripley's function analysis on the same experimental data.

As a matter of fact, the very nature of the model allows one to assess shear and tensile behaviors during fracture propagation in contrast with continuum models where smear cracks over a region and are unable to capture local oriented events. In general, the LDPM facets are subject to both tensile and shear strains even though the test configuration is designed for mode I opening. One can look at the evolution of the dissipated energy computed from the increment of the dissipated energy density $\dot{w}_d = 3(t_N \dot{e}_N^{ine} + t_M \dot{e}_M^{ine} + t_L \dot{e}_L^{ine})$ for $e_N > 0$ and the volume of the cell I containing the facet $V_I = (\sum_k A_k^p l_k)/3$. Summing over the entire volume of the sample, one can obtain the evolution in time (or displacement here) of the total dissipated energy W_d and dissociate the individual contributions of the normal component $W_{d,N}$ and the tangential components $W_{d,T}$. In the present simulations, $W_{d,N}$ almost coincides with the energy dissipated in tension. Figures 5(j)-(l) show the load-displacement curves for the beams with the size $D = 100$ mm for the three different notch lengths, together with the dissipated energies. As expected, the total energy dissipated at the end of the test/simulation is smaller for the larger notch length, i.e. for a smaller ligament length. This is consistent with the acoustic energy obtained from acoustic emission on the same type of experiments reported in the work of Grégoire et al. (2015).

Moreover, one can observe a sharper increase in the dissipated energy as the notch length decreases, which is consistent with the increase in brittleness as α tends to zero. Up to the peak load, the energy dissipated in shear is negligible as compared to the one in tension, for all cases including the unnotched beam. However in the post-peak regime, the energy dissipated in shear becomes more than half of the energy dissipated in tension, which proves that the post-peak behavior involves both shear and tensile forces in the meso-structure.

5.2.3. *Quality of predictions*

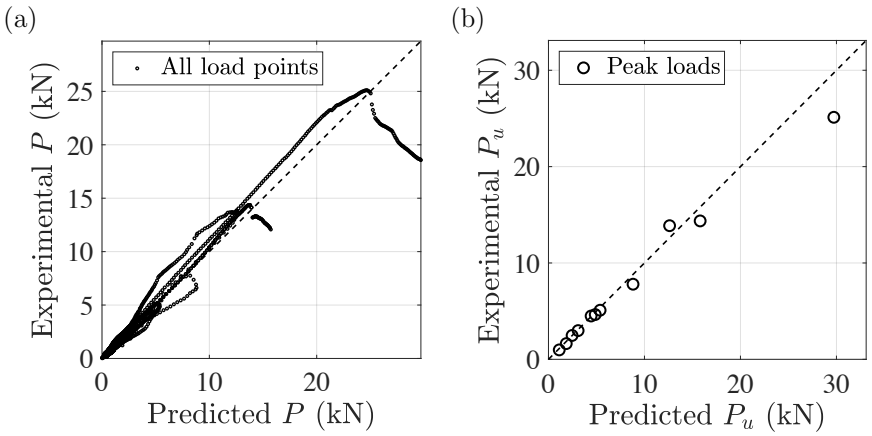

Figure 6: Statistics of the model predictions: (a) scatter of the measured versus predicted values of loads, and (b) scatter of the measured versus predicted values of the peak loads only. The dashed lines correspond to the 1:1 lines.

The quality of predictions was also assessed. Figure 6(a) shows the scatter between experimental and numerical loads for all geometries and sizes, on the entire load-displacement curves. Figure 6(b) shows the same scatter but only for the peak values. In both figures, the cloud of points are close to the 1:1 lines. The set of load points that deviate the most to the 1:1 lines corresponds to the largest unnotched beam (Figure 6(a)). The prediction overestimates the peak load by about 15% (Figure 6(b)). One might be tempted to invoke statistical size-effect related to the randomness in material properties, which is not captured by the deterministic version of LDPM used in this study. Such an effect can be effectively simulated by introducing random fields on the mesoscale model parameters as performed in the work of Eliáš and Vořechovskỳ (2020). Nevertheless, the deterministic predictions are inaccurate only for the unnotched beam of size $D = 400$ mm. Further testing on larger unnotched beam sizes would help validate or invalidate a possible statistical effect for beam with the size $D = 400$ mm. In addition, the use of random fields would add a new level of complexity by making the inverse parameter identification problem ill-conditioned with respect to the limited reported experimental data.

Overall, a coefficient of determination of $r^2 = 0.94$ and a coefficient of variation of

$\omega = 36.8\%$ were found when all load points are considered. For the peak loads only, the values of $r^2 = 0.95$ and $\omega = 23.5\%$ were obtained. The values of the coefficients of variation show that the numerical predictions are very reasonable and are within the typical scatter observed in concrete fracture testing. These results demonstrate quantitatively the capability of the model to predict the effects of size and geometry during concrete failure.

5.3. Universal size-effect law and fracture parameters

Macroscopic properties of concrete such as compressive or tensile strength are usually determined in laboratory using standardized sample dimensions. On the other hand, size-effect tests applied in a certain range of sizes were shown to provide an accurate estimation of fracture properties (RILEM, 1990). This method is preferred to the work of fracture method that provides apparent fracture properties which are geometry and size dependent. The size-effect method only requires the knowledge of peak loads and sample geometry (Bažant and Planas, 1997). It appears therefore interesting to compare the fracture parameters obtained using experimental results as reported by Grégoire et al. (2013) and parameters one could identify using the numerical predictions, keeping in mind that only one load-CMOD curve on a single size notched beam was sufficient for model calibration.

For this purpose, many approximated formulae exist and can be used (Morel, 2008; Cusatis and Schauffert, 2009; Bažant and Yu, 2009; Di Luzio and Cusatis, 2018; Chen and Hu, 2022). Typically, two parameters are enough to capture size-effect in notched three-point bending tests (RILEM, 1990; Planas et al., 1997; Cusatis and Schauffert, 2009; Chen and Hu, 2022). Unnotched specimens can also be simulated but the size cannot be too large as statistical size-effect becomes non-negligible (Eliáš et al., 2015). In this study, the so-called Universal Size Effect Law (USEL) in its deterministic version (Bažant and Yu, 2009) was considered. This fitting formula bridges Type I size-effect which occurs in structures that fail at crack initiation from a smooth surface and Type II size-effect occurring in notched structures. It also covers the two distinct asymptotic behaviors at large size in the typical double-logarithm nominal strength versus structural size representation: (i) 1/2 slope corresponding to linear elastic fracture mechanics for Type II size-effect and (ii) a

straight horizontal line corresponding to the elastic limit for Type I size-effect. The formula is written as:

$$\sigma_{Nu} = \sqrt{\frac{EG_f}{g_0' c_f + g_0 D}} \left(1 - \frac{r c_f^2 g_0'' e^{-k\alpha^2}}{4(l_p + D)(g_0 D + g_0' c_f)} \right)^{1/r} \tag{11}$$

where $\sigma_{Nu} = (3P_u S)/(2WD^2)$ is the nominal strength corresponding to the peak load P_u, G_f is the fracture energy , and c_f is the effective length of the FPZ. $g_0 = g(\alpha_0)$ is the dimensionless energy release rate, and $g_0' = g'(\alpha_0)$ and $g_0'' = g''(\alpha_0)$ are its first and second derivatives, respectively, evaluated at the initial notch-to-depth ratios $\alpha_0 = 0.5, 0.2, 0$. Finally, r, k, and l_p are empirical constants. Based on the expression of $g(\alpha)$ reported for example by Bažant and Planas (1997) or Grégoire et al. (2013), the following values were computed for the geometry studied in this paper: $g_0 = 2.96$, $g_0' = 18.95$, and $g_0' = 153.88$ for $\alpha = 0.5$, $g_0 = 0.57$, $g_0' = 3.17$, and $g_0'' = 10.77$ for $\alpha = 0.2$, and $g_0 = 0$, $g_0' = 3.41$, and g_0'' =-16.75 for $\alpha = 0$. By keeping the empirical constants $r = 0.11$, $k = 113$, and $l_p = 12.9$ identical to the ones reported in the work of Grégoire et al. (2013), the model was fitted using the simulation data. The values of the fracture energy and effective length, $G_f = 39$ N m^{-1} and $c_f = 16.8$ mm were obtained with a coefficient of determination $r^2 = 0.97$ and a coefficient of variation of $\omega = 1.82\%$. Figures 7(a)-(b) show the fitted model plotted together with the experimental and numerical data.

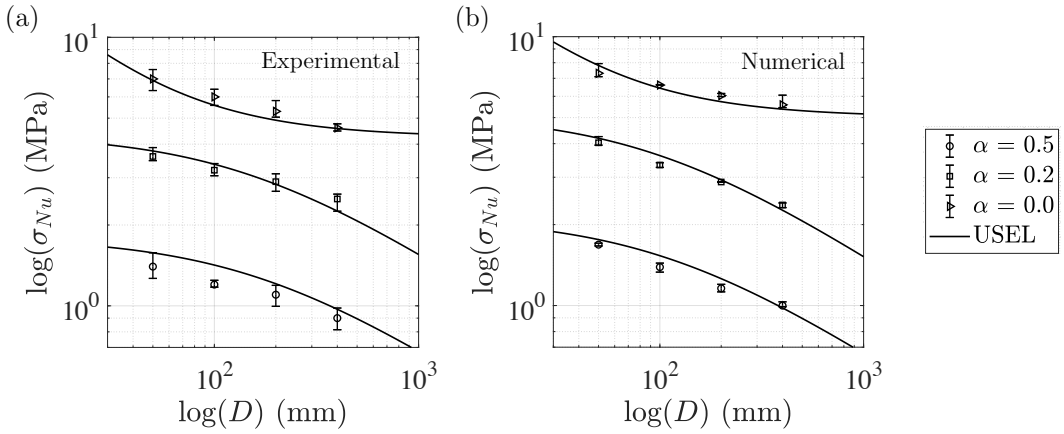

Figure 7: Fitting with the Universal Size Effect Law: nominal strength versus size for (a) experimental data and (b) simulation results.

These predicted fracture parameters are to be compared with the ones identified using

the experimental results, i.e. $G_f = 42.6$ N m^{-1} and $c_f = 25.7$ mm (Grégoire et al., 2013): both fracture energy and effective length can be qualitatively considered close enough with respect to the scatter of typical experiments on concrete. This result suggests that one could perform only one fracture test on a specific geometry in the laboratory, calibrate and use LDPM to simulate different sizes (and possibly geometries) to finally identify the fracture energy and effective length of the FPZ through a size-effect law.

6. Conclusions

In this study, a large set of experimental results on fracture and size-effect including the effect of geometry was simulated using the Lattice Discrete Particle Model (LDPM). The load-CMOD curve of a single size notched beam under three-point bending, and the compressive strength were used for model calibration. The remaining experimental results, namely one splitting test and eleven three-point bending tests of different beam sizes and notch lengths, were used for model validation without parameter adjustment. The fracturing process was discussed along with a rigorous quantification of quality of fit and quality of predictions. Fracture parameters using the numerical results were identified through the Universal Size Effect Law (USEL). Based on the obtained results the following conclusions can be drawn:

- The compressive strength and the load-CMOD curve of a single notched beam size are sufficient for a complete model calibration in elastic, tensile and tensile-shear behaviors.
- The predictions on splitting tests and on the different beam geometries and sizes are overall in excellent agreement with the experimental data.
- The fracturing process is well captured by LDPM for both notched and unnotched beams.
- The dissipated energy in shear constitutes a large part of the total dissipated energy in the post-peak.

- The fracture energy can be estimated through a size-effect law by using the simulation results.
- The use of a stochastic model does not seem to be justified with respect to the limited range of beam sizes.

7. Declarations of interest

The Authors declare that there is no conflict of interest.

8. Acknowledgment

Partial financial support from the investissement d'avenir French programme (ANR-16-IDEX-0002) under the framework of the E2S UPPA hub Newpores and from the Ezponda project under the FEDER program is gratefully acknowledged. This research was supported in part through the computational resources provided for the Quest high performance computing facility at Northwestern University which is jointly supported by the Office of the Provost, the Office for Research, and Northwestern University Information Technology.

9. Appendix

9.1. LDPM constitutive equations for pore collapse, compaction, and frictional behavior

The pore collapse and material compaction occur for $e_N < 0$. Strain hardening plasticity behavior due to high compressive hydrostatic deformation is computed through a strain-dependent boundary $\sigma_{bc}(e_D, e_V)$ at each facet which limits the normal compressive stress component via the inequality $-\sigma_{bc}(e_D, e_V) \leqslant t_N \leqslant 0$, in which the volumetric strain is defined as $e_V = \Delta V/(3V_0)$, computed as the change between the current and the initial volume of each LDPM tetrahedron. While e_V is the same for all the facets of a given tetrahedron, the deviatoric strain defined as $e_D = e_N - e_V$ changes. Finally, the strain-dependent boundary is calculated for three different cases $\sigma_{bc}(e_D, e_V) = \sigma_{c0}$ for $-e_V \leq 0$, $\sigma_{bc}(e_D, e_V) = \sigma_{c0} + \langle -e_V - \varepsilon_{c0} \rangle H_c(r_{DV})$ for $0 \leq -e_V \leq e_{c1}$ and $\sigma_{bc}(e_D, e_V) = \sigma_{c1}(r_{DV}) \exp\left[(-e_V - e_{c1})H_c(r_{DV})/\sigma_{c1}(r_{DV})\right]$ otherwise, where $r_{DV} = |e_D|/e_V$ for $e_V > 0$

and $r_{DV} = -|e_D|/(e_V - e_{V0})$ for $e_V \leq 0$ in which $e_{V0} = \kappa_{c3} e_{c0}$. $e_{c0} = \sigma_{c0}/E_0$ defines σ_{c0} the mesoscale yielding compressive stress, $e_{c1} = \kappa_{c0} e_{c0}$ is the strain at which the rehardening starts, κ_{c0} and κ_{c3} are material constants and $\sigma_{c1}(r_{DV}) = \sigma_{c0} + (e_{c1} - e_{c0}) H_c(r_{DV})$. The function $H_c(r_{DV})$ reads as $H_c(r_{DV}) = H_{c1} + (H_{c0} - H_{c1})/(1 + \kappa_{c2}\langle r_{DV} - k_{c1}\rangle)$ where H_{c0}, H_{c1}, κ_{c1} and κ_{c2} are material constants.

The frictional behavior due to compression-shear occurs also for $e_N < 0$. In the presence of compressive stresses, the shear strength increases due to frictional effects. The frictional behavior is simulated by means of a nonlinear Mohr-Coulomb model in which the internal friction coefficient varies from an initial value μ_0 to zero. The formulation can be written as $\sigma_{bs} = \sigma_s + \mu_0 \sigma_{N0} - \mu_0 \sigma_{N0} \exp(\sigma_N/\sigma_{N0})$ where σ_s is the cohesion stress and σ_{N0} is the transitional stress.

References

ACI-Committee, 2019. Building code requirements for structural concrete (aci 318-19) and commentary. American Concrete Institute.

Alnaggar, M., Cusatis, G., Di Luzio, G., 2013. Lattice discrete particle modeling (ldpm) of alkali silica reaction (asr) deterioration of concrete structures. Cement and Concrete Composites 41, 45–59.

Angiolilli, M., Gregori, A., Pathirage, M., Cusatis, G., 2020. Fiber reinforced cementitious matrix (frcm) for strengthening historical stone masonry structures: Experiments and computations. Engineering Structures 224, 111102.

Angiolilli, M., Pathirage, M., Gregori, A., Cusatis, G., 2021. Lattice discrete particle model for the simulation of irregular stone masonry. Journal of Structural Engineering 147 (9), 04021123.

Barbat, G., Cervera, M., Chiumenti, M., Espinoza, E., 2020. Structural size effect: Experimental, theoretical and accurate computational assessment. Engineering Structures 213, 110555.

Bažant, Z. P., Le, J.-L., 2017. Probabilistic Mechanics of Quasibrittle Structures: Strength, Lifetime, and Size Effect. Cambridge University Press.

Bažant, Z. P., 2002. Scaling of Structural Strength. CRC Press.

Bažant, Z. P., Jirásek, M., 2002. Nonlocal integral formulations of plasticity and damage: survey of progress. Journal of Engineering Mechanics 128 (11), 1119–1149.

Bažant, Z. P., Oh, B. H., 1983. Crack band theory for fracture of concrete. Materials and Structures 16 (3), 155–177.

Bažant, Z. P., Pfeiffer, P. A., 1987. Determination of fracture energy from size effect and brittleness number. ACI Materials Journal 84 (6), 463–480.

Bažant, Z. P., Planas, J., 1997. Fracture and Size Effect in Concrete and Other Quasibrittle Materials. CRC press.

Bažant, Z. P., Yu, Q., 2009. Universal size effect law and effect of crack depth on quasi-brittle structure strength. Journal of Engineering Mechanics 135 (2), 78–84.

Bolander, J. E., Eliáš, J., Cusatis, G., Nagai, K., 2021. Discrete mechanical models of concrete fracture. Engineering Fracture Mechanics 257, 108030.

Çağlar, Y., Şener, S., 2016. Size effect tests of different notch depth specimens with support rotation measurements. Engineering Fracture Mechanics 157, 43–55.

Chen, Y., Hu, X., 2022. On interchangeability and selection of size effect and boundary effect experiments for characterization and prediction of quasi-brittle fracture of concrete. Theoretical and Applied Fracture Mechanics 122, 103629.

Cibelli, A., Pathirage, M., Cusatis, G., Ferrara, L., Di Luzio, G., 2022. A discrete numerical model for the effects of crack healing on the behaviour of ordinary plain concrete: Implementation, calibration, and validation. Engineering Fracture Mechanics 263, 108266.

Cusatis, G., Pelessone, D., Mencarelli, A., 2011a. Lattice discrete particle model (ldpm) for failure behavior of concrete. i: Theory. Cement and Concrete Composites 33 (9), 881–890.

Cusatis, G., Mencarelli, A., Pelessone, D., Baylot, J., 2011b. Lattice discrete particle model (ldpm) for failure behavior of concrete. ii: Calibration and validation. Cement and Concrete Composites 33 (9), 891–905.

Cusatis, G., Schauffert, E. A., 2009. Cohesive crack analysis of size effect. Engineering Fracture Mechanics 76 (14), 2163–2173.

Di Luzio, G., Cusatis, G., 2018. Cohesive crack analysis of size effect for samples with blunt notches and generalized size effect curve for quasi-brittle materials. Engineering Fracture Mechanics 204, 15–28.

Eliáš, J., Vořechovskỳ, M., 2020. Fracture in random quasibrittle media: I. discrete mesoscale simulations of load capacity and fracture process zone. Engineering Fracture Mechanics 235, 107160.

Eliáš, J., Vořechovskỳ, M., Skoček, J., Bažant, Z. P., 2015. Stochastic discrete meso-scale simulations of concrete fracture: Comparison to experimental data. Engineering Fracture Mechanics 135, 1–16.

Elices, M., Guinea, G., Gomez, J., Planas, J., 2002. The cohesive zone model: advantages, limitations and challenges. Engineering Fracture Mechanics 69 (2), 137–163.

Feng, J., Sun, W., Chen, L., Chen, B., Arkin, E., Du, L., Pathirage, M., 2022. Engineered cementitious composites using chinese local ingredients: Material preparation and numerical investigation. Case Studies in Construction Materials 16, e00852.

Grassl, P., Grégoire, D., Solano, L. R., Pijaudier-Cabot, G., 2012. Meso-scale modelling of the size effect on the fracture process zone of concrete. International Journal of Solids and Structures 49 (13), 1818–1827.

Grégoire, D., Rojas-Solano, L. B., Pijaudier-Cabot, G., 2013. Failure and size effect for notched and unnotched concrete beams. International Journal for Numerical and Analytical Methods in Geomechanics 37 (10), 1434–1452.

Grégoire, D., Verdon, L., Lefort, V., Grassl, P., Saliba, J., Regoin, J.-P., Loukili, A., Pijaudier-Cabot, G., 2015. Mesoscale analysis of failure in quasi-brittle materials: comparison between lattice model and acoustic emission data. International Journal for Numerical and Analytical Methods in Geomechanics 39 (15), 1639–1664.

Han, L., Pathirage, M., Akono, A.-T., Cusatis, G., 11 2020. Lattice discrete particle modeling of size effect in slab scratch tests. Journal of Applied Mechanics 88 (2), 021009.

Hoover, C. G., Bažant, Z. P., Vorel, J., Wendner, R., Hubler, M. H., 2013. Comprehensive concrete fracture tests: description and results. Engineering Fracture Mechanics 114, 92–103.

Lefort, V., Pijaudier-Cabot, G., Grégoire, D., 2015. Analysis by ripley's function of the correlations involved during failure in quasi-brittle materials: Experimental and numerical investigations at the mesoscale. Engineering Fracture Mechanics 147, 449–467.

Li, W., Rezakhani, R., Jin, C., Zhou, X., Cusatis, G., 2017. A multiscale framework for the simulation of the anisotropic mechanical behavior of shale. International Journal for Numerical and Analytical Methods in Geomechanics 41 (14), 1494–1522.

Mercuri, M., Pathirage, M., Gregori, A., Cusatis, G., 2020. Computational modeling of the out-of-plane behavior of unreinforced irregular masonry. Engineering Structures 223, 111181.

Mercuri, M., Pathirage, M., Gregori, A., Cusatis, G., 2021. On the collapse of the masonry medici tower: An integrated discrete-analytical approach. Engineering Structures 246, 113046.

Mercuri, M., Pathirage, M., Gregori, A., Cusatis, G., 2022. Masonry vaulted structures under spreading supports: Analyses of fracturing behavior and size effect. Journal of Building Engineering 45, 103396.

Morel, S., 2008. Size effect in quasibrittle fracture: derivation of the energetic size effect law from equivalent lefm and asymptotic analysis. International journal of fracture 154 (1), 15–26.

Nguyen, H., Pathirage, M., Rezaei, M., Issa, M., Cusatis, G., Bažant, Z. P., 2020a. New perspective of fracture mechanics inspired by gap test with crack-parallel compression. Proceedings of the National Academy of Sciences 117 (25), 14015–14020.

Nguyen, H. T., Pathirage, M., Cusatis, G., Bažant, Z. P., 05 2020b. Gap Test of Crack-Parallel Stress Effect on Quasibrittle Fracture and Its Consequences. Journal of Applied Mechanics 87 (7), 071012.

Pathirage, M., Bentz, D., Di Luzio, G., Masoero, E., Cusatis, G., 2019a. The onix model: a parameter-free multiscale framework for the prediction of self-desiccation in concrete. Cement and Concrete Composites

103, 36–48.

Pathirage, M., Bousikhane, F., D'Ambrosia, M., Alnaggar, M., Cusatis, G., 2019b. Effect of alkali silica reaction on the mechanical properties of aging mortar bars: Experiments and numerical modeling. International Journal of Damage Mechanics 28 (2), 291–322.

Pathirage, M., Thierry, F., Tong, D., Cusatis, G., Grégoire, D., Pijaudier-Cabot, G., 2022a. Comparative investigation of dynamic implicit and explicit methods for the lattice discrete particle model. In: Computational Modelling of Concrete and Concrete Structures. CRC press, pp. 503–509.

Pathirage, M., Tong, D., Thierry, F., Cusatis, G., Grégoire, D., Pijaudier-Cabot, G., 2022b. Numerical modeling of concrete fracturing and size-effect of notched beams. In: Computational Modelling of Concrete and Concrete Structures. CRC press, pp. 496–502.

Pijaudier-Cabot, G., Toussaint, D., Pathirage, M., Grégoire, D., Vermorel, R., Cusatis, G., 2022. Surface and size effects on elasticity and fracture. In: Computational Modelling of Concrete and Concrete Structures. CRC Press, pp. 46–55.

Planas, J., Guinea, G., Elices, M., 1997. Generalized size effect equation for quasibrittle materials. Fatigue & Fracture of Engineering Materials & Structures 20 (5), 671–687.

Rezakhani, R., Scott, D. A., Bousikhane, F., Pathirage, M., Moser, R. D., Green, B. H., Cusatis, G., 2021. Influence of steel fiber size, shape, and strength on the quasi-static properties of ultra-high performance concrete: Experimental investigation and numerical modeling. Construction and Building Materials 296, 123532.

RILEM, D. R., 1990. Size-effect method for determining fracture energy and process zone size of concrete. Materials and Structures 23, 461–465.

Rocco, C. G., 1996. Influencia del tamaño y mecanismos de rotura del ensayo de compresión diametral. Ph.D. thesis, Universidad Politecnica de Madrid.

Schauffert, E. A., Cusatis, G., 2011. Lattice discrete particle model for fiber-reinforced concrete. i: Theory. Journal of Engineering Mechanics 138 (7), 826–833.

Yang, L., Pathirage, M., Su, H., Alnaggar, M., Di Luzio, G., Cusatis, G., 2021. Computational modeling of temperature and relative humidity effects on concrete expansion due to alkali–silica reaction. Cement and Concrete Composites 124, 104237.

Yang, L., Pathirage, M., Su, H., Alnaggar, M., Di Luzio, G., Cusatis, G., 2022. Computational modeling of expansion and deterioration due to alkali–silica reaction: Effects of size range, size distribution, and content of reactive aggregate. International Journal of Solids and Structures 234-235, 111220.

Zhu, Z., Pathirage, M., Wang, W., Troemner, M., Cusatis, G., 2022. Lattice discrete particle modeling of concrete under cyclic tension–compression with multi-axial confinement. Construction and Building Materials 352, 128985.